frontiers | Frontiers in Earth Science

TYPE Original Research
PUBLISHED 12 September 2022
DOI 10.3389/feart.2022.990187

OPEN ACCESS

EDITED BY
Wenjun Zheng,
School of Earth Sciences and Engineering, Sun Yat-sen University, China

REVIEWED BY
Junjie Ren,
Institute of Crustal Dynamics, China Earthquake Administration, China
Hu Wang,
Southwest Jiaotong University, China
Chuanyong Wu,
Institute of Disaster Prevention, China

*CORRESPONDENCE
Lichun Chen,
glutclc@glut.edu.cn

SPECIALTY SECTION
This article was submitted to Structural Geology and Tectonics, a section of the journal Frontiers in Earth Science

RECEIVED 09 July 2022
ACCEPTED 11 August 2022
PUBLISHED 12 September 2022

CITATION
Han M, Chen L, Li Y, Gao S and Feng J (2022), Paleoearthquakes of the Yangda-Yaxu fault across the Nujiang suture and Lancang river suture zone, southeastern Tibetan Plateau. *Front. Earth Sci.* 10:990187. doi: 10.3389/feart.2022.990187

Paleoearthquakes of the Yangda-Yaxu fault across the Nujiang suture and Lancang river suture zone, southeastern Tibetan Plateau

Mingming Han[1,2], Lichun Chen[3]*, Yanbao Li[1], Shuaipo Gao[1] and Jiahui Feng[1]

[1]Institute of Geology, China Earthquake Administration, Beijing, China, [2]Chengdu Center of China Geological Survey, Chengdu, China, [3]College of Earth Sciences, Guilin University of Technology, Guilin, China

The WNW-trending Yangda-Yaxu fault (YYF) is located in the interior of the Qiangtang block (QTB). The YYF cuts through the Nujiang suture and Lancang river suture zone and divides Nujiang fault (NF) and Lancangjiang fault (LCJF) into two sections with significantly different activity levels, suggesting that the YYF may function as a specific structure in this region. In addition, a recent work argues that the YYF plays an important role in strain partitioning in southeastern Tibet and poses a high surface-faulting risk to the Sichuan-Tibet railway. However, no $M \geq 5.0$ earthquakes have been recorded, and no palaeoseismic research has been conducted along the fault, leading to limited knowledge regarding its rupture behavior, which is essential for understanding regional tectonic deformation and assessing the regional seismic potential. In this study, we constrained the timings and recurrence intervals of late Quaternary paleoseismic events along the YYF for the first time. Through trench excavations and exposure cleaning combined with radiocarbon dating, five faulting events were identified, namely, E1 through E5 from youngest to oldest (831–1,220, 3,307–6,703, 9,361–10,286, 12,729–14,651, and before 14,651 yr BP). The recurrence interval of major earthquakes along the YYF follows a quasi-periodic pattern with an interval of ~4,000 yr. Combining the clear linear geomorphic features along the fault and the paleoearthquake results in this paper, we believe that YYF is a newly-generated active fault, and has a significant control effect on the late Quaternary evolution of the NF and the LCJF. Further analysis revealed that the YYF also plays an important role in accommodating crustal deformation.

KEYWORDS

Yangda-Yaxu fault, Nujiang suture zone, paleoearthquake, active fault, newly-generated fault, Tibetan Plateau (TP)

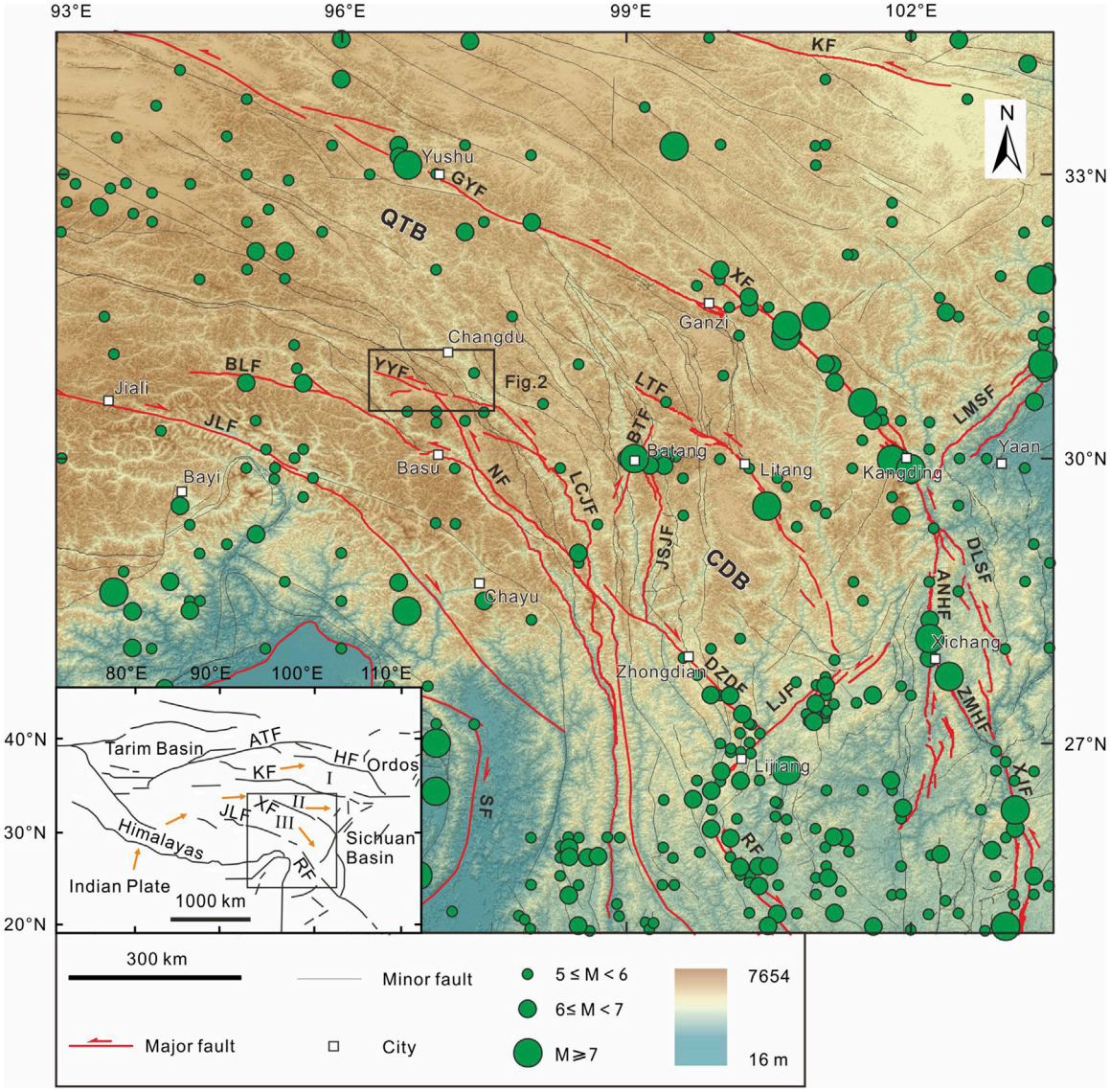

FIGURE 1
Regional tectonics and seismicity in southeastern Tibet. The red lines are major active fault traces. The green circles of different sizes indicate epicenters of earlier documented (historical and instrumental) earthquakes. The small white rectangles denote cities. The black rectangle indicates the study area of the YYF. QTB, Qiangtang block; CDB, Chuandian block. The hillshade map is generated from the Advanced Spaceborne Thermal Emission and Reflection Radiometer (ASTER) Global Digital Elevation Model (ASTGTM) (90-m resolution). Index map showing major boundary faults and blocks on the Tibetan Plateau. The orange arrows indicate the block motion direction according to GPS data (Gan et al., 2007). Blocks: I, Qaidam-Qilian block; II, Bayan Har block; III, Qiangtang-Chuandian block. Abbreviations of the active faults: ATF, Altyn Tagh fault; HF, Haiyuan fault; XF, Xianshuihe fault; JLF, Jiali fault; RF, Red River fault; BLF, Bianba-Luolong fault; YYF, Yangda-Yayu fault; NF, Nujiang fault; LTF, Litang fault; LCJF, Lancangjiang fault; JSJF, Jinshajiang fault; BTF, Batang fault; LMSF, Longmenshan fault; DLSF, Daliangshan fault; ANHF, Anninghe fault; ZMHF, Zemuhe fault; XJF, Xiaojiang fault; LJF, Lijiang-Xiaojinhe fault; DZDF, Deqin-Zhongdian-Daju fault; SF, Sagaing fault.

1 Introduction

Collision and continued convergence of the Indian and Eurasian plates have led to rapid Cenozoic uplift and intense crustal deformation (Yin and Harrison, 2000; Tapponnier et al., 2001). To accommodate uplift and crustal deformation on the southeastern Tibetan Plateau, a large number of faults have been generated or reactivated, resulting in a very seismically active region (Figure 1; Yin and Harrison, 2000; Deng et al., 2002; Xu et al., 2003; Zhang et al., 2003; Taylor and Yin, 2009). In this region, historical documents and instruments have recorded more than 40 $M \geq 6.7$ earthquakes over the past

century (Li et al., 2019), most of which occurred along the boundary faults of tectonic blocks, such as the NW-SE-trending Xianshuihe fault (XF) and the NS-trending Xiaojiang fault (XJF) (Wang et al., 2013; Li et al., 2019; Guo et al., 2021). Because of the frequent occurrence of large earthquakes, these faults have stimulated great interest to geoscientists and have been considered important in accommodating crustal deformation of the Tibetan Plateau (Allen et al., 1991; Tapponnier et al., 2001; Wang et al., 2020; Guo et al., 2021). In contrast, few studies have considered the faults within active blocks; accordingly, the seismic risk and role in strain partitioning of these faults have generally been neglected. Over the past hundred years, a number of strong earthquakes, such as the 1933 *M* 7.5 Diexi earthquake (Ren et al., 2018), 1947 *M* 7¾ Dari earthquake (Liang et al., 2020a), 1948 *Ms* $7^1/_4$ Litang earthquake (Xu et al., 2005a), and 2021 *Mw* 7.3 Maduo earthquake (Ren et al., 2022a), have successively occurred along intrablock faults, indicating that the secondary faults within active blocks also exhibit the potential to produce devastating earthquakes and can play a role in strain partitioning (Zhan et al., 2021; Ren et al., 2022b; Yuan et al., 2022). As a consequence, investigation of the rupture behavior of these faults is vital not only to assess the regional seismic potential but also to better understand the deformation mechanism of tectonic blocks (Ren et al., 2013; Sun et al., 2015; Sun et al., 2017).

The Yangda-Yaxu fault (YYF), generally trending WNW, terminating at the Lancangjiang fault (LCJF) in the east, is one of the faults within the Qiangtang block (QTB). The YYF exhibits distinct linear features and faulted landforms revealed *via* image interpretation and field investigation studies. In addition, the YYF cuts through the Nujiang suture and Lancang river suture zone and divides Nujiang fault (NF) and Lancangjiang fault (LCJF) into two sections with significantly different activity levels, suggesting that the YYF may function as a specific structure in this region (Han, 2022a). However, for a long time, the fault geometry and Quaternary activity have remained poorly understood because of a lack of field data due to poor transportation conditions and high elevation, in addition to a lack of strong earthquake records. Recently, Ren et al. (2022b) first studied the geometric distribution and activity of the YYF *via* remote sensing interpretation, field investigation and chronological analysis. Further analysis revealed that the YYF has played an essential role in strain partitioning in eastern Tibet, and its presence poses a seismic potential on the Sichuan-Tibet railway, which traverses eastern Tibet and crosses the YYF (Ren et al., 2022b). However, until now, no paleoseismological investigation has been conducted, and little is known regarding the paleoearthquake history of the YYF, resulting in significant uncertainty in assessing the regional seismic potential and understanding its role in accommodating crustal deformation in eastern Tibet. Therefore, it is very crucial to investigate the faulting behavior and paleoearthquake history of the YYF.

In this paper, to constrain the rupture history of the YYF, we conducted field investigations and trench excavations based on the interpretation of high-resolution satellite images combined with radiocarbon dating. Then, we compared the latest Quaternary faulting behavior and kinematic properties of the YYF to those of neighboring faults. Finally, we described the tectonic implications of intrablock faults in seismic hazard assessment and regional strain partitioning.

2 Regional seismotectonic setting

The Qiangtang block (QTB) and Chuandian block (CDB) are being extruded south-southeastward, rotating clockwise around the Eastern Himalayan syntaxis, due to the ongoing collision of the Indian and Eurasian plates (Tapponnier et al., 2001; Xu et al., 2003; Zhang et al., 2004; Gan et al., 2007; Wang and Shen, 2020). Two groups of active faults with different strikes of nearly NEN and NW-WNW are located in the eastern QTB and northwest CDB (Figure 1).

The nearly NEN-striking fault mainly comprises the Batang fault (BTF). Six earthquakes of $M \geq 6.0$ have occurred along the BTF in recorded history (Department of Earthquake Disaster Prevention and State Seismological Bureau., 1995). Among these recorded earthquakes, the 1870 *M* $7^1/_4$ Batang earthquake, which was the largest earthquake, produced a right-lateral surface rupture zone (Xu et al., 2005b; Zhou et al., 2005), with a maximum right-lateral offset of 1.5 m, and a maximum vertical offset of 0.6 ± 0.2 m (Xu et al., 2005b). The late Quaternary strike-slip rate of the BTF has been estimated *via* geological methods as 1.3–2.7 mm/yr (Zhou et al., 2005). Recent trench work revealed that several surface-rupturing events have occurred during the late Quaternary, among which the latest event corresponds to the 1870 *M* $7^1/_4$ Batang earthquake (Gao, 2021). The activity of the BTF was weak during the early Holocene, increasing significantly since the late Holocene, and the recurrence interval was shortened to approximately 830 yr, as revealed *via* further analysis.

The nearly NW-WNW-striking faults mostly include the XF, Jiali fault (JLF), Deqin-Zhongdian-Daju fault (DZDF), Litang fault (LTF), Bianba-Luolong fault (BLF) and YYF (Figure 1). The left-lateral strike-slip XF, located along the northern boundary of the CDB, is seismically highly active, where more than ten large earthquakes ($Ms \geq 6.9$) occurred in recorded history (Allen et al., 1991; Wen et al., 2008). Based on multiple measurements, the strike-slip rate of the fault has been estimated to be ~2.5–5.6 mm/yr (Li et al., 2017; Liang, 2019; Liang et al., 2020b; Gao, 2021). Previous trench excavations have revealed that several paleoearthquakes have occurred since the Holocene, specifically, five events in the Qianning segment over the past ~9,000 yr (Li et al., 2017), six events in the Luhuo segment over the past ~3,000 yr (Liang et al., 2020b). The seismic sequences of the Luhuo and Qianning segments are consistent with clustering

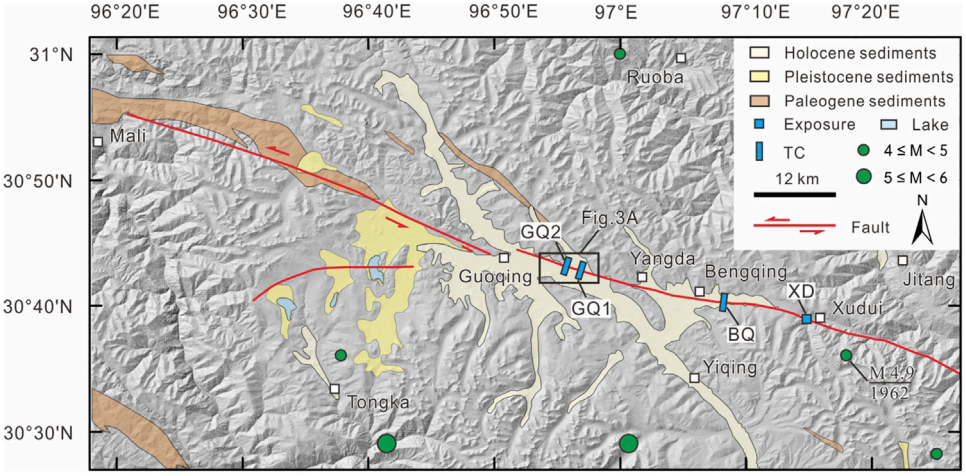

FIGURE 2
Geologic features and fault distribution of the YYF. Please refer to location in Figure 1. Geological data are adapted from the 1:250000 geologic map. The hillshade map is generated from the ASTGTM (30-m resolution). The black box indicates the extent of Figure 3A.

and abnormal accelerating stress release behavior patterns (Li et al., 2017; Liang et al., 2020b). The recent research data based on faulted landforms, paleoseismic trenches and GPS data reveal that the JLF is generally a Holocene active fault with dextral strike-slip and thrust component (Wang et al., 2020; Zhang et al., 2021). The fault has experienced at least two strong earthquake events since the Holocene (Wang et al., 2020), the latest of which occurred between 2,680–2,160 yr BP. The dextral strike-slip rate is about 2.4–3.8 mm/yr (Zhang et al., 2021). DZDF is characterized by dextral strike-slip with normal. The horizontal slip rate of the fault since Holocene is 1.7–2.0 mm/yr, and the vertical slip rate is 0.6–0.7 mm/yr (Chang et al., 2014).

The LTF, which is mostly parallel to the XF, is also quite active, with three historical earthquakes of M >7 since 1700 (Zhou et al., 2015; Chevalier et al., 2016; Wang et al., 2021). Among these earthquakes, the 1890 Mw ~7.3 earthquake produced a surface rupture zone with a length of ~71 km (Wang et al., 2021), and the latest large earthquake occurred in 1948 (Ms $7^1/_4$) with an ~40-km surface rupture (Xu et al., 2005a). The LTF is a dominantly left-lateral strike-slip fault with a late Quaternary strike-slip rate of ~2–4 mm/yr, as evidenced *via* geological and dating investigations (Xu et al., 2005a; Zhou et al., 2005, 2007; Gao, 2021; Wang et al., 2021). Recent trench excavations have revealed that four paleoseimic events have occurred since the Holocene, and the recurrence intervals were ~1,415 yr, ~1,104 yr, and ~775 yr (Wang et al., 2021). Historical records indicate that two large earthquakes, namely, the 1,642–1,654 M ≥7 Luolong earthquake and the 1,791–1,804 M $6^3/_4$ Bianba earthquake (Science and Technology Committee of the Tibetan Autonomous Region, 1982; Department of Earthquake Disaster Prevention and State Seismological Bureau, 1995), have occurred along the BLF. A recent study based on the field survey and ^{14}C dating methods has suggested that the BLF is a Holocene active fault with the latest faulting event possibly corresponding to the 1,642–1,654 M ≥ 7 Luolong earthquake, and the main movement pattern of the fault is sinistral strike-slip movement (Han et al., 2022b). The YYF is mainly a left-lateral strike-slip fault with a horizontal rate of ~1.7 mm/yr during the late Quaternary, as evidenced from displaced landforms integrated with corresponding dating results (Ren et al., 2022b). The clear surface ruptures, notable surface cracks and sand liquefaction phenomenon suggest that the last earthquake along the YYF did not occur long ago (Ren et al., 2022b). However, the YYF experienced very low seismic activity. Historic records indicate no M ≥ 5.0 earthquakes along the YYF. The largest earthquake was the 1971 M 4.9 earthquake (Figure 2). Furthermore, small–moderate earthquakes with a magnitude less than 5.0 rarely occur along the fault, although the possibility that this phenomenon is also related to the sparse seismic stations in the adjacent areas cannot be ruled out. To date, no paleoearthquake sequence along the YYF since the late Quaternary has been reported.

3 Materials and methods

3.1 Field investigation and trench analysis

The surface traces of the YYF (Figure 2) were mapped in detail based on high-resolution Google Earth image interpretation and field investigation of faulted landforms, including fault scarps, fault troughs, sag ponds, alluvial fans, gullies, streams, and surface ruptures. To reveal fault

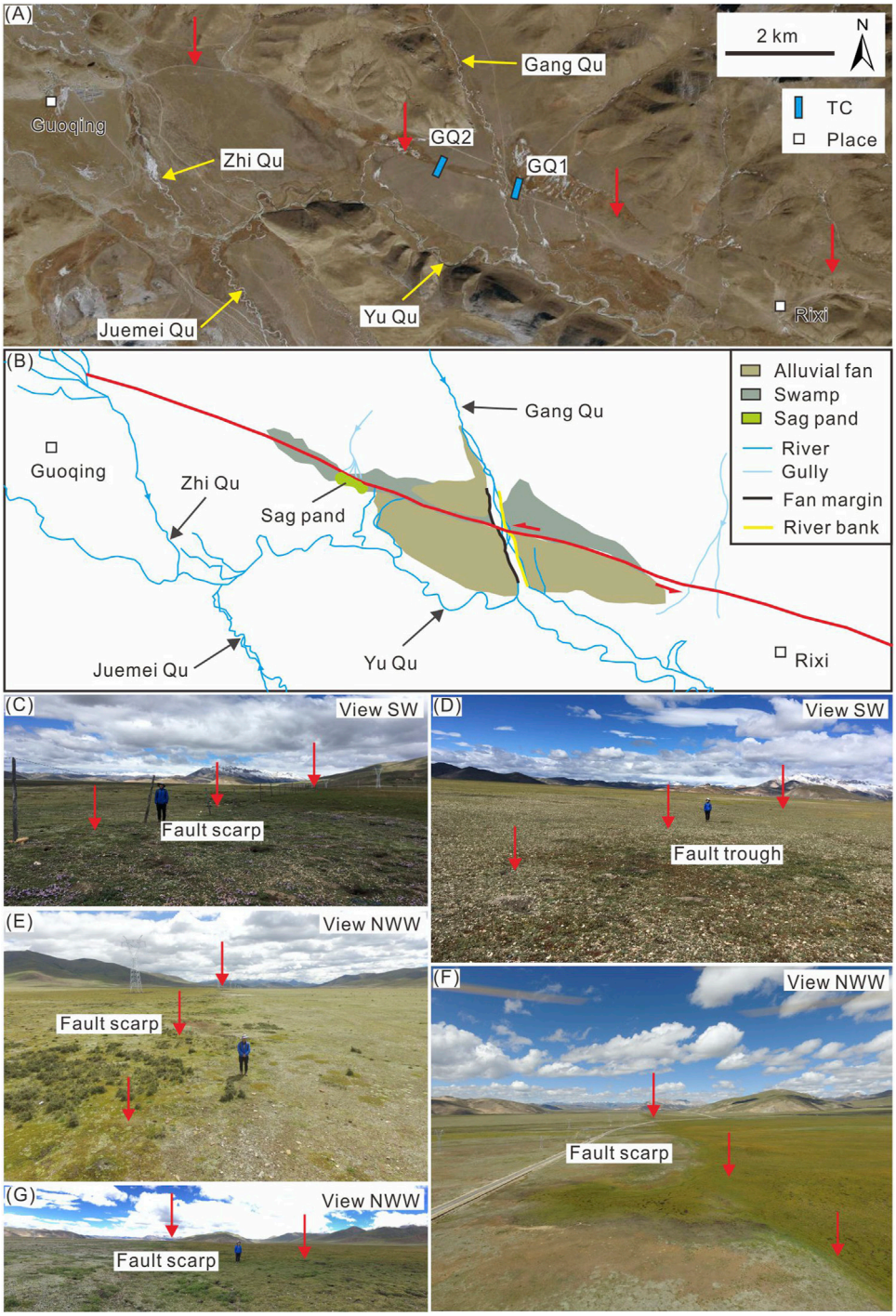

FIGURE 3
Fault traces and faulted landforms near the Guoqing township and the locations of trenches GQ1 and GQ2. **(A)** Satellite image and **(B)** interpreted map of the offset landforms near the Guoqing township. The location is shown in Figure 2. The red arrows and lines point to the surface traces of the fault. **(C–G)** Field photographs of the fault traces and representative faulted landforms.

structures and paleoseismic evidence, three trenches were excavated nearly perpendicular to the fault traces (Figure 3). Trench excavation sites were selected based on locations where sediments were relatively continuous and stable, such as sag ponds or small depressions across distinct fault scarps. Unmanned aerial vehicle-based

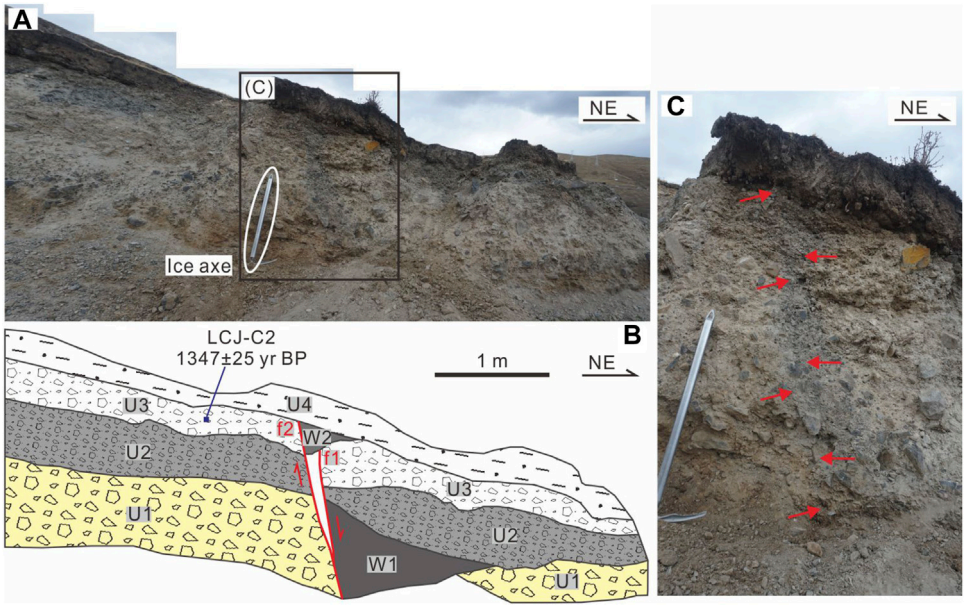

FIGURE 4
(A) Photograph and **(B)** interpreted sketch of the XD fault exposure. The location is shown in Figure 14C. **(C)** Enlarged photograph of the local details of the fault exposure. The U and red lines indicate the stratum units and the fault plane, respectively.

photogrammetry was employed to finely measure offset landforms at the trench sites and produce high-resolution digital elevation models (Bemis et al., 2014; Gao et al., 2017). The walls of each trench were systematically cleaned to expose clear evidence of paleoseismic events. After trench walls cleaning, 1 m by 1 m grids were constructed to capture photos. Field logging was conducted involving square gridded paper, and the field logs were then digitalized on a computer. In addition, along the YYF, a fault exposure, which was suitably exposed near Xudui village due to human activity, was cleaned and analyzed (Figures 3, 4).

3.2 Radiocarbon dating

Numerous radiocarbon samples were collected from the faulted and unfaulted strata in the three trenches and one outcrop. The ^{14}C samples were processed and analyzed by Beta Analytic Inc. Detailed accelerometer mass spectrometry (AMS) ^{14}C sample preparation was provided by Beta Analytic Inc.; please refer to their website (https://www.radiocarbon.cn/beta-AMS-lab/). The ages of the samples were corrected as two-sigma calendar ages (95.4% confidence interval) with the OxCal 4.4 procedure (Ramsey, 2009; Reimer et al., 2013). The timings of the determined paleoseismic events based on the considered trenches and outcrop were also limited using the progressive confining method considering the sample age.

4 Paleoseismic investigation

4.1 Guoqing site

4.1.1 Site location and offset landforms

In the eastern part of the Guoqing township, the YYF cuts through piedmont alluvial fans, forming a well-extended linear scarp and a gentle trough landform on the surface. Moreover, a small sag pond is locally developed (Figures 3A,B). The trend of the linear scarp ranges from ~280 to 290°, and the height of the scarp ranges from ~0.6 to 1.7 m (Figures 5D–G, 6B). There are obvious differences in turf growth conditions between both sides of the scarp, and linear swamps are developed in low-lying areas near the scarp (Figure 3). In addition, due to fault motion, the sinistral offset occurs at the fan margin of the alluvial fan, Gang Qu (Qu means river in Chinese) river banks and several small gullies (Figure 3B), with a displacement ranging from ~20 to 40 m (Ren et al., 2022b). To reveal the complete sequence of paleoseismic events as much as possible, this paper excavated two trenches across the local low-lying area of the linear scarp (Figures 5A-B, 6A,C), denoted as trenches GQ1 and GQ2, from east to west, which were approximately 2 km away from each other (Figures 2, 3A).

4.1.2 Stratigraphy

Trench GQ1 is approximately 18 m long, 3 m wide, and 3 m deep (Figure 5C). Trench GQ2 is approximately 19 m long, 3 m wide, and 3 m deep (Figure 6D). Both the western and eastern walls of GQ1 and GQ2 exhibit a similar stratigraphy and

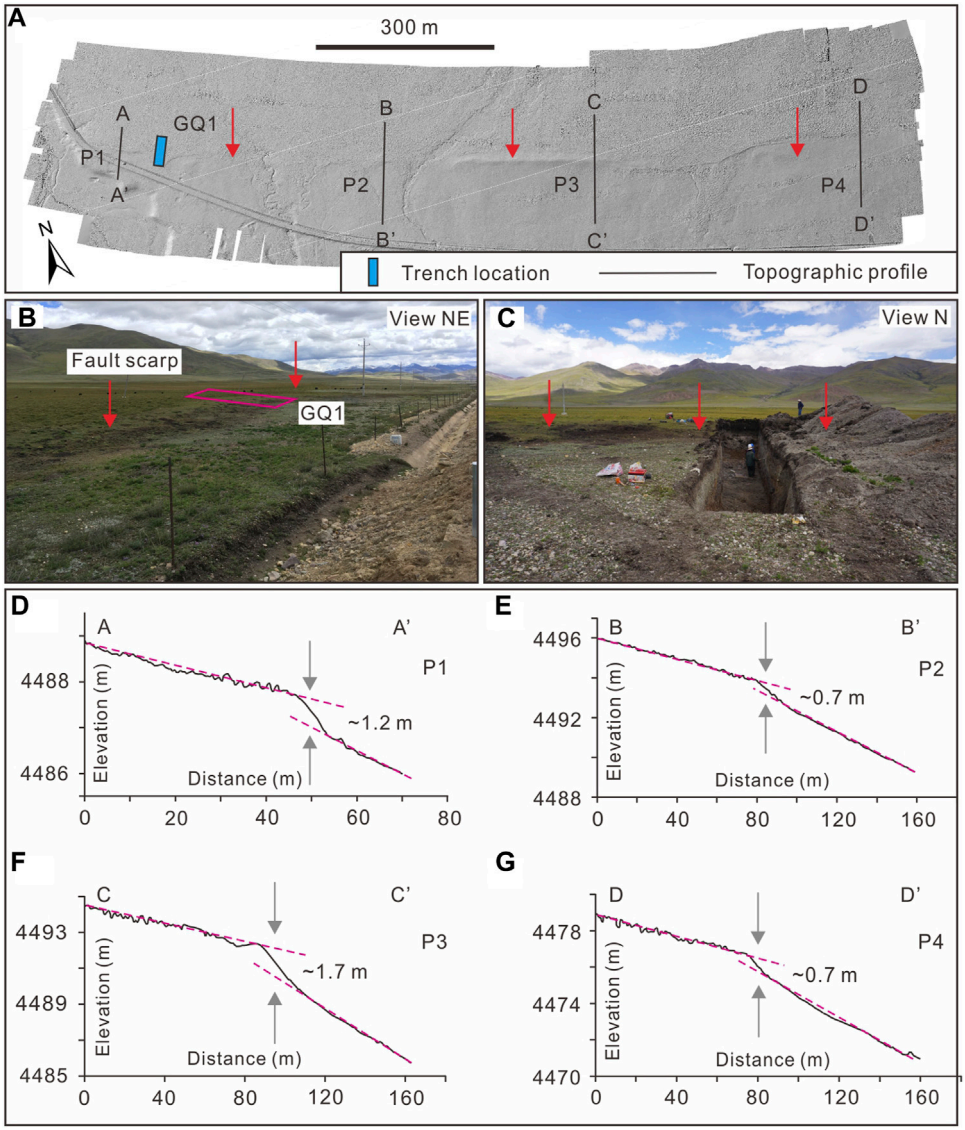

FIGURE 5
Faulted landforms around the trench GQ1 excavation site. **(A)** The hillshade map is generated from an unmanned aerial vehicle-based digital elevation model. The location is shown in Figure 3A. The red arrows point to the surface trace of the fault. **(B,C)** Field photos of the fault scarp and location of trench GQ1. **(D–G)** P1–P4 topographic profiles across the fault scarp.

deformation features. The strata mainly comprise alluvial gravel layers at the bottom and clay or sandy clay layers at the top, typical of fluvial facies. Five units of layers, including nine subunits, named in ascending order from bottom to top, could be recognized in the trenches sections (Figures 7, 8, 9). The description of these strata are provided in Tables 1, 2.

4.1.3 Evidence for events in trench GQ1

Based on the gravel alignment and deformation and lithological differences among the various strata, eight faults, namely, f1–f8, and seven faults, namely, f1–f7, from the northeast to the southwest, could be identified in the eastern trench wall (Figure 7) and western trench wall (Figure 8), respectively. Specifically, on the eastern wall, these fault planes steeply dipped and formed a typical flower structure, which is common in strike-slip fault zones. On the western wall, the fault planes, as a whole, were subparallel. Based on analysis of the deformed strata and corresponding cut-and-cover structures and paleoseismic markers (Liu-Zeng et al., 2007; McCalpin, 2009; Ran et al., 2012; Wang et al., 2013; Wang et al., 2020; Guo et al.,

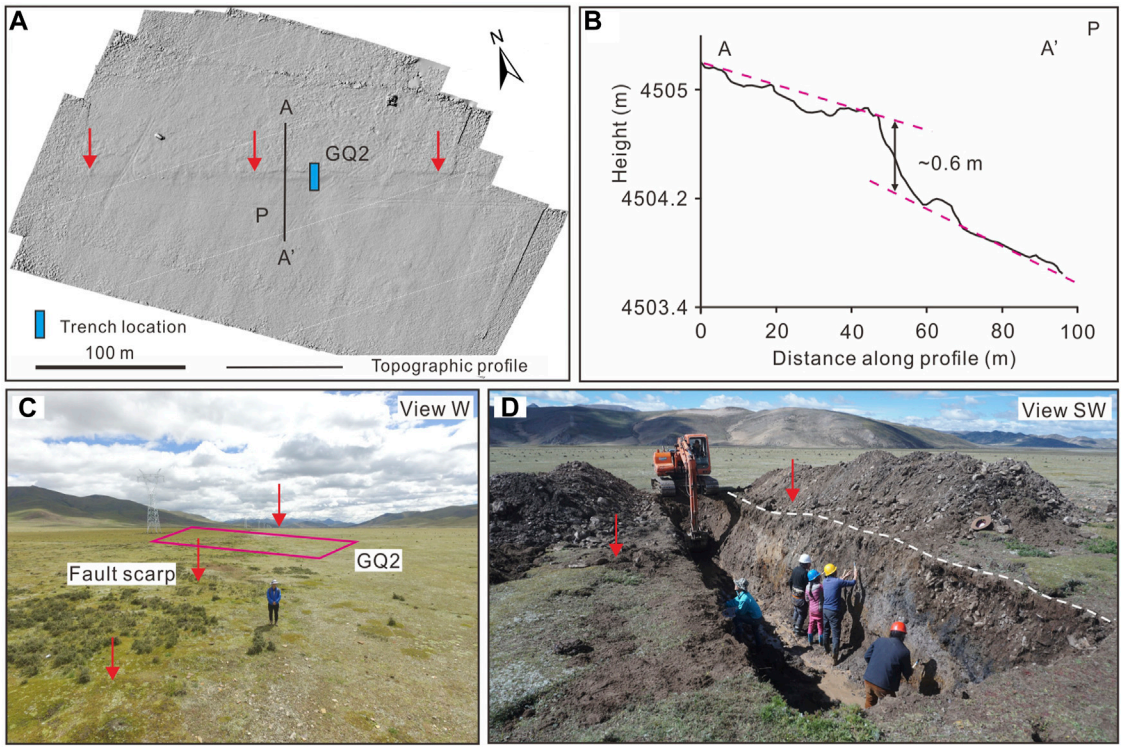

FIGURE 6
Faulted landforms around the trench GQ2 excavation site. **(A)** The hillshade map is generated from an unmanned aerial vehicle-based digital elevation model. The location is shown in Figure 3A. The red arrows point to the surface trace of the fault. **(B)** P topographic profile across the fault scarp. **(C,D)** Field photos of the fault scarp and location of trench GQ2.

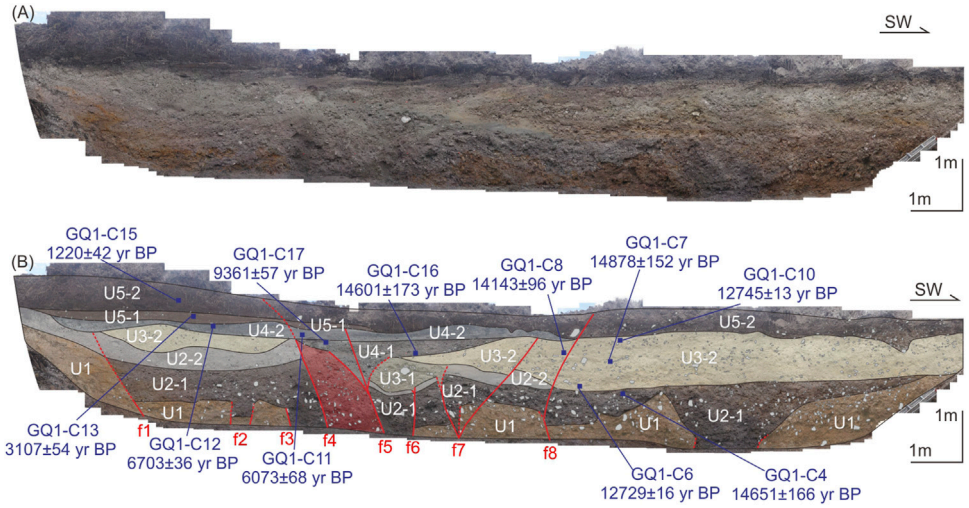

FIGURE 7
Photomosaic **(A)** and interpretation map **(B)** of the eastern wall of trench GQ1.

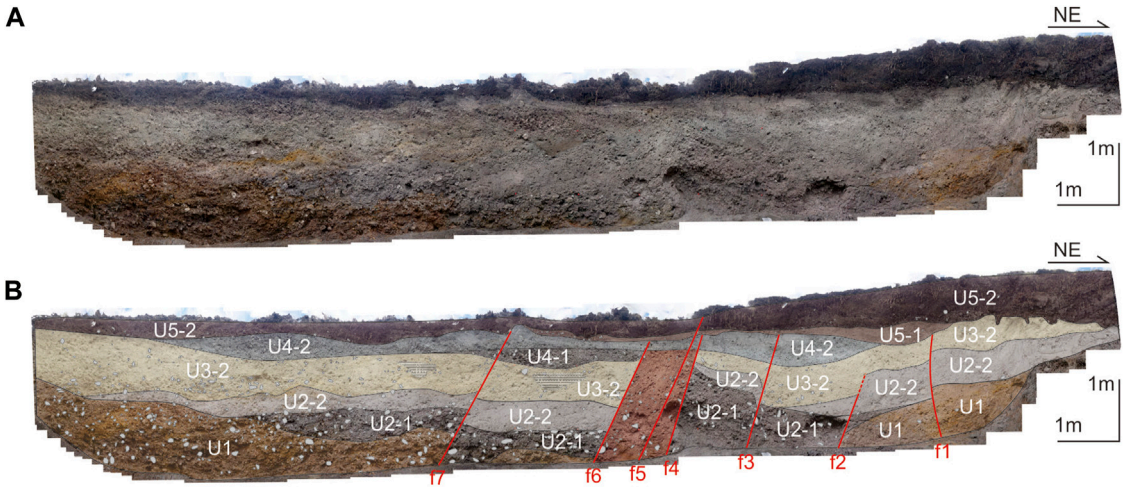

FIGURE 8
Photomosaic **(A)** and interpretation map **(B)** of the western wall of trench GQ1.

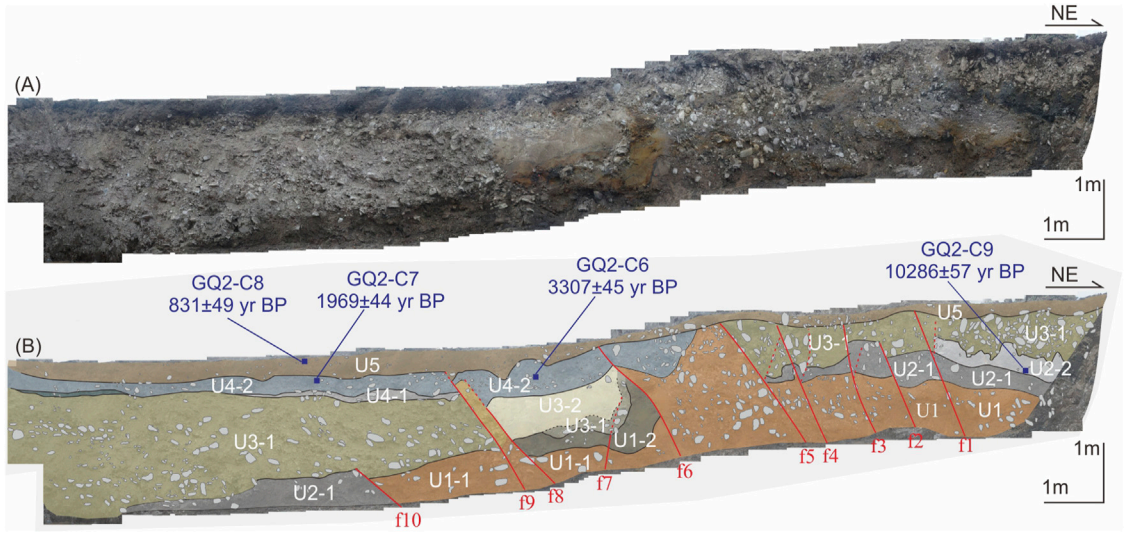

FIGURE 9
Photomosaic **(A)** and interpretation map **(B)** of the western wall of trench GQ2.

2021), five paleoearthquakes were identified, denoted as G1E1, G1E2, G1E3, G1E4, and G1E5, from youngest to oldest.

4.1.3.1 Event G1E5

This event was mainly revealed on the eastern wall (Figure 7). Faults f3, f2, middle branch of f7, and northeast branch of f8 faulted layer U1, which were overlain by layer U2-1, resulting in a faulted contact between layers U2-1 and U1. In conclusion, the event EGO5 occurred after U1 deposition and before U2-1 deposition.

4.1.3.2 Event G1E4

Western wall fault f2 faulted layer U2-2, overlain by layer U3-2, resulting in layer U3-2 occurring in unconformable contact with U2-2 (Figure 8). Eastern wall faults f6 and northeast branch of f7 faulted layer U2-2 and were overlain by U3-1 (Figure 7). Faulting and traction of f6 and f7-1 led to strong tilting deformation of U2-2 than that of the strata on both sides. Thus, the above evidence indicates that event EGO4 occurred between the deposition of layers U2-2 and U3-1.

TABLE 1 Unit description of trench GQ1.

Unit	Description
U1	Yellow–brown gravel layer containing a small amount of clay, with a certain sedimentary bedding. The gravel particles are angular
U2-1	Light gray–green gravel layer, mixed deposits. The gravel particles are angular
U2-2	Sandy clay layer with a high sand content, the color is mainly gray
U3-1	Gravel interbedded with clay layers. Versicolor mixed deposits, mainly gray–green. The gravel particles are well sorted. Gravel particles with a size of 3–5 cm are dominant, and the largest particles are up to 10 cm in size. This layer may be associated with multiple material sources
U3-2	Gray–green fine sandy clay layer containing a small amount of fine gravel particles. The gravel particles are angular
U4-1	Gravel interbedded with clay, the color is mainly brownish red
U4-2	Silty clay layer with local bedding, the color is mainly gray–black
U5-1	Thin layer of small gravel particles. This stratum is developed locally near the fault, with the characteristics of frontal fault scarp deposition
U5-2	Gray–black modern root soil layer. There is a small amount of small-sized gravel particles, and a few large gravel particles up to 13 cm in size

TABLE 2 Unit description of trench GQ2.

Unit	Description
U1-1	Gravel layer, containing a small amount of sand. The color is mainly gray–green to brown–green, with a slight light–yellow hue. The gravel particles are poorly rounded and exhibit obvious directional arrangement along the fault planes
U1-2	Gray–black to gray–green clay interbedded with a gravel layer. This stratum exhibits notable disturbance. The gravel particles are poorly sorted and poorly rounded
U2-1	Brown–green sand-gravel layer. The gravel particles are angular or subangular
U2-2	Sand layer with occasional gravel, and the bottom contains black strips with strong deformation.
U3-1	Gravel layer, the color is mainly gray–white. The gravel particles are poorly sorted and poorly rounded
U3-2	Thin layer of sand interbedded with clay, developed locally, containing a small amount of gravel particles
U4-1	Gray–green gravel layer, developed locally
U4-2	Black silty clay layer, containing a small amount of small gravel particles. The thickness is variable with a limited distribution.
U5	Gray–black topsoil layer rich in plant roots, containing a small amount of small gravel particles. Some large gravel particles are only visible near the fault at the northern end of the eastern wall.

4.1.3.3 Event G1E3

This event was mainly revealed on the eastern wall (Figure 7). Southwest branch of f7 faulted layer U3-2 and was overlain by U4-2. In addition, southwest branch of f5 faulted layer U3-1 and was overlain by U4-1. Therefore, event EGO3 occurred after the deposition of U3-2 and before the deposition of U4-1.

4.1.3.4 Event G1E2

On the eastern wall, the middle branch of fault f5 faulted layer U4-2, overlain by U5-1 (Figure 7). On the western wall, faults f3, f4, and f6 faulted layer U4-2 and was overlain by U5-1. Fault f7 faulted U4-2 and was overlain by U5-2 (Figure 8). Therefore, event EGO2 occurred between the deposition of U4-2 and U5-1.

4.1.3.5 Event G1E1

Western wall fault f5 and eastern wall faults f8 and f4 faulted layer U5-2 and extended to the ground surface (Figures 7, 8). A well-preserved fault scarp at this location was interpreted to have been formed by this event. Based on the above, the EGO1 occurred after U5-2 deposition, which may correspond to a historical earthquake.

4.1.4 Evidence for events in trench GQ2

Similarly, ten fault branches were identified, denoted as f1–f10 from northeast to southwest (Figure 9). Based on analysis of the paleoseismic markers, three paleoseismic events were identified, namely, G2E1, G2E2, and G2E3, from youngest to oldest.

4.1.4.1 Event G2E3

Faults f2 and f10 faulted layer U2-1, overlain by layer U3-1. Along the above fault planes, there occurred multiple aligned small gravel particles. Therefore, these observations show that event EGT3 occurred before deposition of U3-1 and after deposition of U2-1.

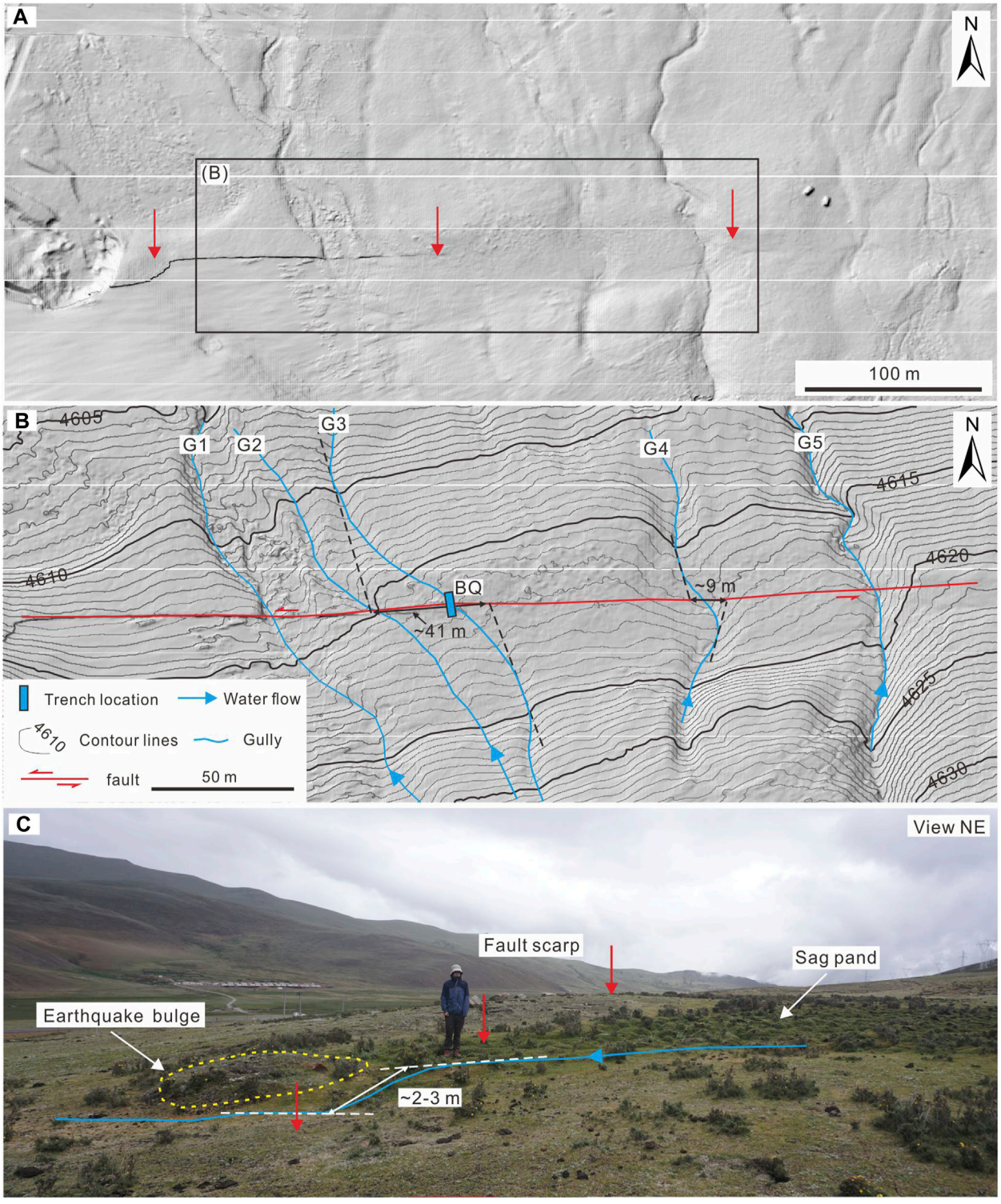

FIGURE 10
Faulted landforms around the trench BQ excavation site. **(A)** The hillshade map is generated from an unmanned aerial vehicle-based digital elevation model. The location is shown in Figure 2. The red arrows point to the surface trace of the fault. **(B)** Interpretation map of the offset landforms in **(A)**. The contour interval is 0.5 m. **(C)** Field photo of the faulted landforms around trench BQ.

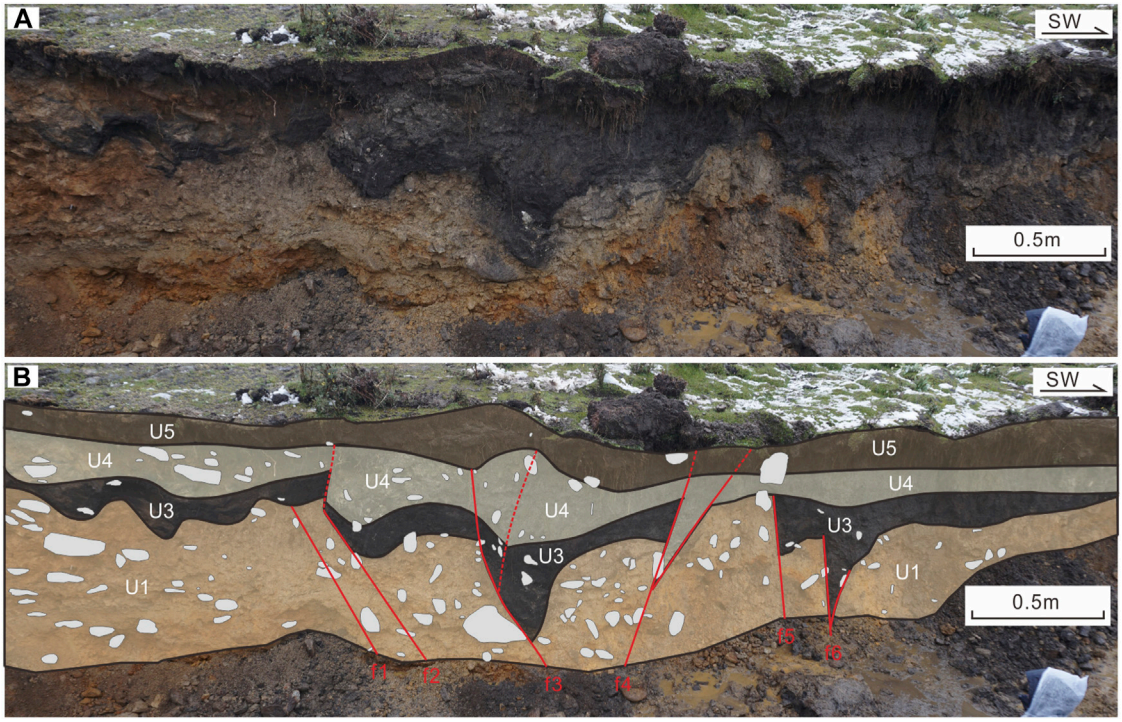

FIGURE 11
Photomosaic **(A)** and interpretation map **(B)** of the eastern wall of trench BQ.

4.1.4.2 Event G2E2

Fault f8 faulted layer U3-2 and was overlain by U4-2. The evidence suggests that event EGT2 occurred before deposition of U4-1 and after deposition of U3-2.

4.1.4.3 Event G2E1

Faults f6 and f9 faulted layer U4-2 and was overlain by U5. No obvious deformation was found in the overlying layer U5. The above evidence indicates that event EGT1 occurred between the deposition of layers U4-2 and U5.

4.2 Bengqing site

4.2.1 Site location and offset landforms

In the southeastern area of Bengqing village, ~21 km away from the trench GQ1 excavation location, the YYF cuts through the piedmont alluvial-proluvial fan (Figure 10A), forming striking faulted landforms, including fault scarps, earthquake bulges, and sag ponds (Figure 10C). Five large gullies (G1–G5) across the fault were synchronously left-laterally offset. The left-lateral displacements of gullies G3 and G4 were ~41 and ~9 m, respectively (Figure 10B). In addition, adjacent to the southern side of the fault scarp and the earthquake bulge, a small gully was dislocated by ~2–3 m, which can represent the horizontal coseismic displacement of the latest earthquake event (Figure 10C).

4.2.2 Stratigraphy

Trench BQ is approximately 13.5 m long, 3 m wide, and 3 m deep. Because of the shallow depth of the ground water table and quick infiltration, in addition to weak properties of the sediments, the northern part of the eastern trench wall collapsed soon after the excavation, and only the southern part was retained. The strata on both walls are similar and hence correlated (Figures 11–13). The strata mainly comprise gravel particles at the bottom and pebbly clays or gravel interbedded clays at the top. Five sets of layers, named in ascending order from bottom to top, could be recognized in the trench sections, among which layer U2 was missing on the eastern wall (Figure 11). A description of the strata is provided in Table 3.

4.2.3 Evidence for events

According to the aligned gravel clasts within the gravel layer and the deformation and lithological differences among the strata, six faults, namely, f1–f6, and three faults, namely, f1–f3, from the northeast to the southwest, could be identified in the eastern trench wall (Figure 11) and western trench wall (Figure 12), respectively. Based on analysis of the deformed strata and paleoseismic markers, four paleoseismic events were identified, namely, BE1, BE2, and BE3, from youngest to the oldest.

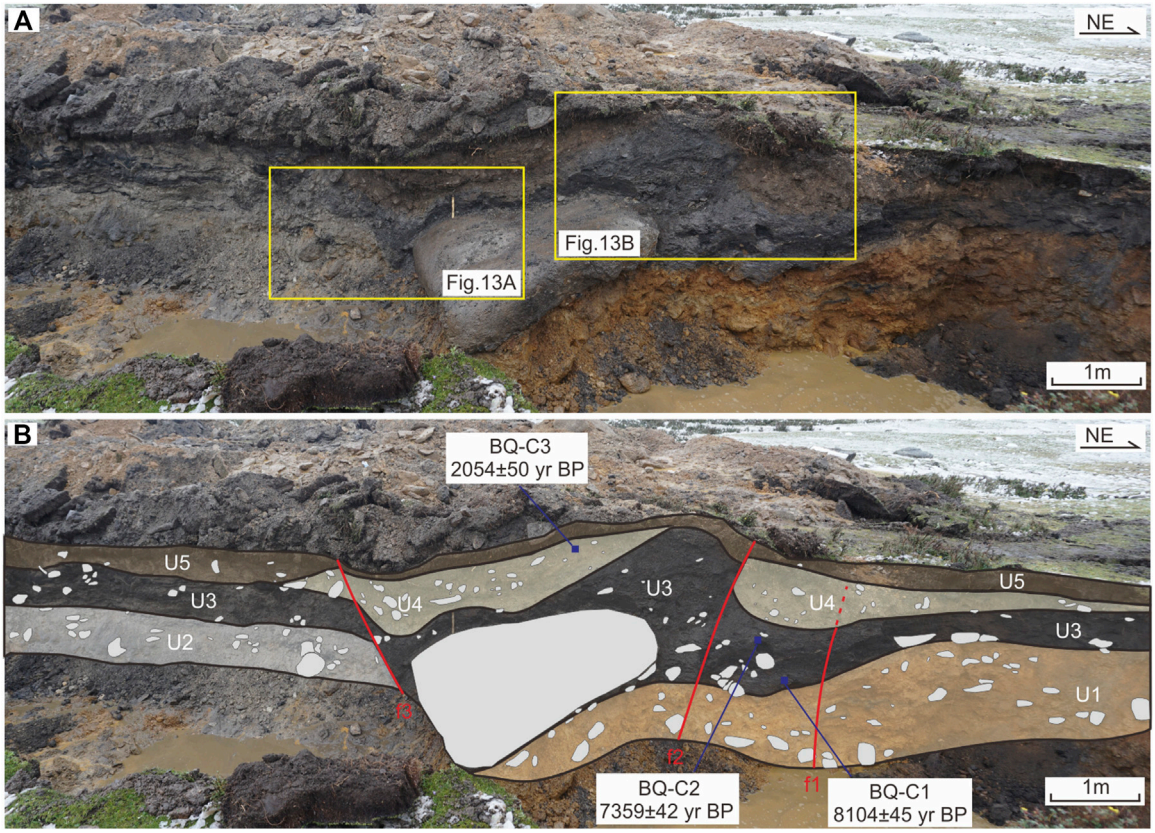

FIGURE 12
Photomosaic **(A)** and interpretation map **(B)** of the western wall of trench BQ.

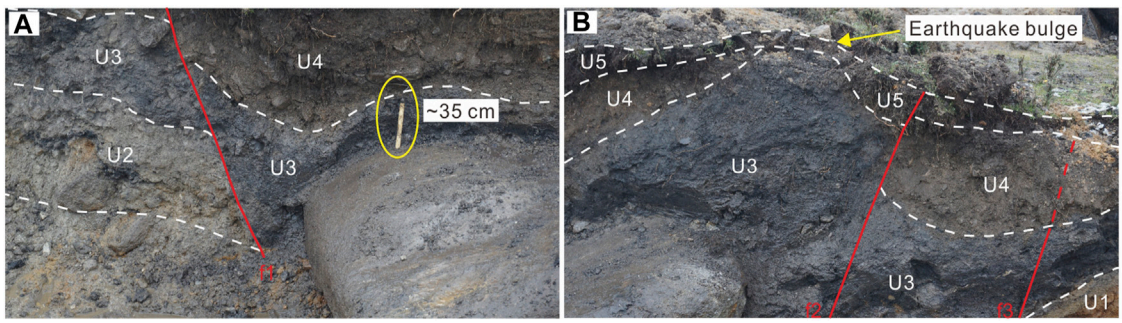

FIGURE 13
Local enlarged photographs of the western wall of trench BQ showing the faulted strata along the faults; the locations are shown in Figure 12A.

4.2.3.1 Event BE3

This event was revealed only on the eastern wall. Faults f1 and f6 faulted layer U1 and was overlain by U3. Along faults f3 and f6, there occurred multiple obvious tensional cracks in the upper part of U1, which were penetrated by U3. In addition, along fault f3, layer U1 exhibited a larger displacement amount and greater top surface disturbance than those exhibited by layer U3 (Figure 11). Therefore, the above evidence suggests that event BE3 occurred after U1 deposition and before U3 deposition.

TABLE 3 Unit description of trench BQ.

Unit	Description
U1	Yellow–brown to yellow–green alluvial-proluvial facies sand-gravel layer mixed with silty sandy clay. The gravel particles are angular and poorly sorted. The gravel particles are oriented along the fault plane near the fault and aligned nearly horizontal far from the fault
U2	Light yellow–brown to yellow–gray gravel-bearing silty clay layer. The gravel particles are angular or subangular and poorly sorted. Only developed locally in the southern part of the western wall
U3	Black clay layer interbedded with gravel. This stratum is strongly disturbed near the fault and relatively stable away from the fault zone. The gravel particles are poorly rounded and aligned near the fault. There are obvious differences in the gravel content and gravel size between the two walls. The eastern wall exhibits a lower content and smaller gravel size, while the western wall exhibits a higher content and larger gravel diameter, and a very large gravel particle occur in the fault zone of the western wall with a gravel diameter of more than 2 m
U4	Gray–black to gray–yellow gravel interbedded with a clay layer. This layer is thick near the fault and gradually thins away from the fault, forming a wedge-shaped deposition with a limited distribution. Gravel is dominant within the fault zone, while clay is dominant far from the fault. The gravel layer comprises mixed deposits and poorly sorted and poorly rounded. This stratum is likely a set of colluvial wedge deposit following an earthquake. The deposition of U4 is likely a colluvial deposit generated by a scarp after an earthquake.
U5	Surface turf layer rich in grass roots, mainly comprising black clay with a small amount of gravel particles

4.2.3.2 Event BE2

On the eastern wall, along fault f2, layer U3 exhibited a larger displacement amount and greater top surface disturbance than those exhibited by layer U4 (Figure 11). On the western wall, layer U4 was locally developed and exhibited a wedge shape, thickening near the fault, and gradually thinning to near-horizontal away from the fault. In layer U4, the gravel particles were mixed, and no horizontal bedding was developed (Figures 12, 13). We could infer that U4 may be a colluvial facies gravel layer formed by event BE2. Therefore, the above evidence indicates that event BE2 occurred after U3 deposition and before U4 deposition.

4.2.3.3 Event BE1

Faults f2 and f3 on the western wall faulted turf layer U5 and ruptured upward to the ground surface (Figure 12). Additionally, fault f4 on the eastern wall appeared to offset layer U5 (Figure 11). The depositional and geomorphological features indicate that event BE1 occurred after U5 deposition and might correspond to a historical earthquake. The well-preserved earthquake bulge was interpreted to have been caused by event BE1 (Figure 13).

4.3 Xudui site

4.3.1 Site location and offset landforms

Near Xudui village, the YYF cuts through the hillside. Satellite images and field investigation revealed that the fault exhibits a linear fault scarp, fault trough and bedrock scarp (Figure 14). Five gullies (G1–G5) were left-laterally offset when crossing the fault (Figure 14B). Close to the west bank of the G4 gully, we cleaned a fault outcrop (Figures 4, 14C), which was widely exposed due to human activity, on the alluvial platform. Here, the exposure was recorded as XD.

4.3.2 Stratigraphy

Exposure XD is approximately 5.5 m long, and 1.5–2 m deep (Figure 4). The strata primarily comprised a sandy gravel layer, typical of the alluvial pluvial phase. Based on the sedimentary characteristics of the strata, four sets of layers, named in ascending order from bottom to top, could be recognized in the cleaned exposure. A description of the strata is provided in Table 4.

4.3.3 Evidence for events and radiocarbon dating of events

Two faults (f1 and f2) with steep dips and normal fault component were identified in the cleaned exposure. Fault f1 merged into fault f2 at the bottom of the exposure, forming a fault zone with a width of ~10 cm. Faulting led to clear gravel orientation and stratigraphic offset, and colluvial wedges were developed near the fault (Figure 4). Based on the cut-and-fill relationship and sedimentary structures, two paleoseismic events were recognized, namely, XE1 and XE2, from youngest to oldest.

4.3.3.1 Event XE2

The older, penultimate event occurred along f1, dislocated sandy gravel layer U1, and resulted in one typical colluvial wedge (W1). Colluvial wedge deposition generally occurred soon after the rupturing event, indicating that the older event occurred between the deposition of layer U1 and wedge W1, shortly before the deposition of W1.

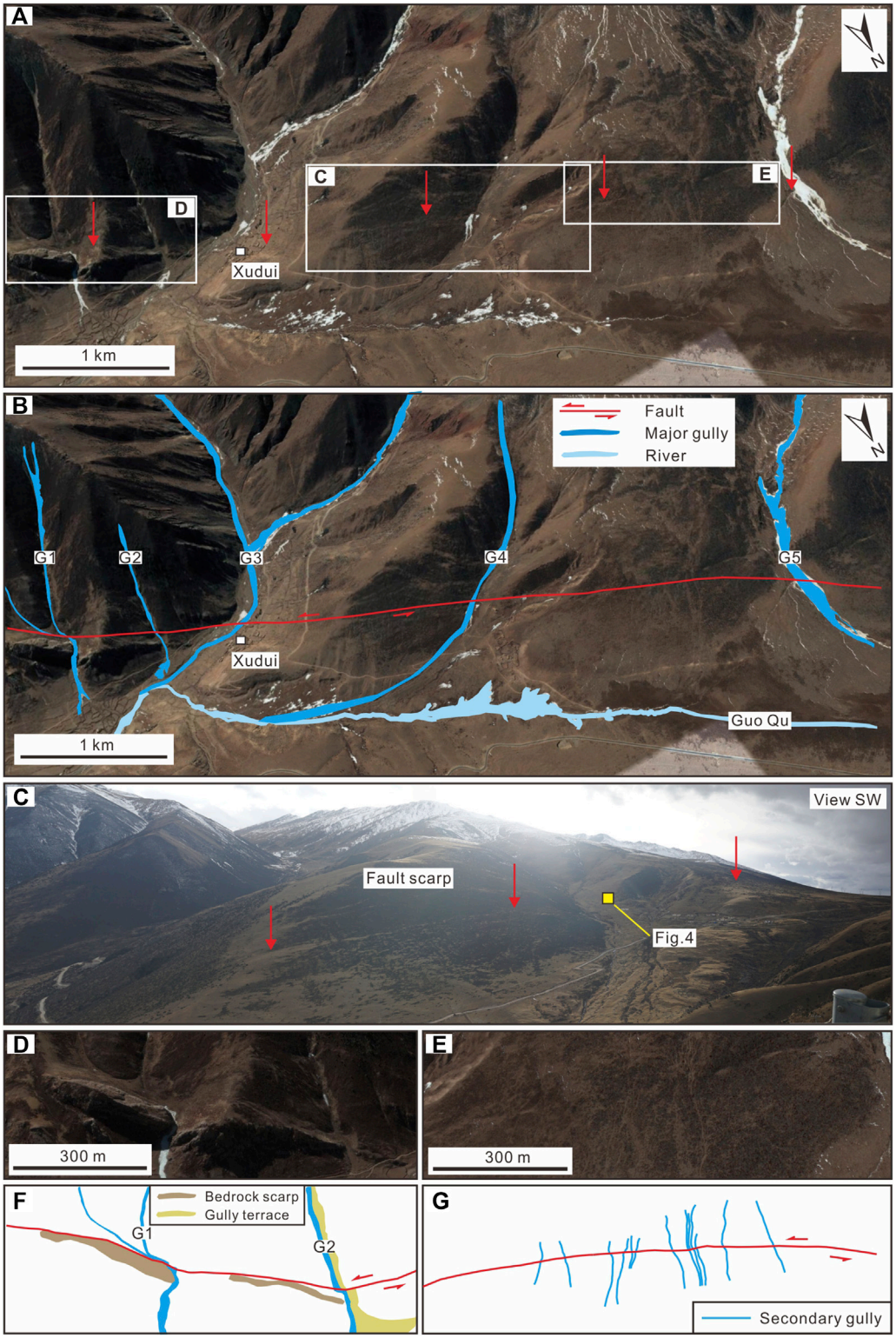

FIGURE 14
Offset landforms around Xudui village and location of the XD fault outcrop. **(A)** Satellite image and **(B)** interpreted map of the tectonic landforms near Xudui village. The location is shown in Figure 2. G1–G5 indicate the major gullies. **(C–E)** Local enlarged photograph of **(A)**. **(F)** Interpretation map of the offset landforms in **(D)**. **(G)** Interpretation map of the offset landforms in **(E)**.

TABLE 4 Unit description of exposure XD.

Unit	Description
U1	Steel–gray sand-gravel layer. The gravel particles are angular
U2	Earthy–yellow sand-gravel layer. The gravel particles are poorly rounded. This layer exhibits a smaller gravel size than that of U1
U3	Steel–gray sand-gravel layer. The gravel particles are poorly rounded
U4	Black soil and turf layer

TABLE 5 Radiocarbon samples and dating results for the three trenches and one outcrop.

Sample	Lab code	Radiocarbon age (yr BP)	Calibration age (cal BP)	Analyzed material	Unit sampled
GQ1-C4	506534	12,480 ± 40	14,651 ± 166	Organic sediment	U2-1, GQ1
GQ1-C6	506536	10,750 ± 40	12,729 ± 16	Organic sediment	U3-2, GQ1
GQ1-C7	506537	12,550 ± 40	14,878 ± 152	Organic sediment	U3-2, GQ1
GQ1-C8	506538	12,220 ± 40	14,143 ± 96	Organic sediment	U3-2, GQ1
GQ1-C10	506539	10,800 ± 30	12,745 ± 13	Organic sediment	U3-2, GQ1
GQ1-C11	506540	5,280 ± 30	6,073 ± 68	Organic sediment	U4-2, GQ1
GQ1-C12	506541	5,880 ± 30	6,703 ± 36	Organic sediment	U4-2, GQ1
GQ1-C13	506542	2,950 ± 30	3,107 ± 54	Organic sediment	U5-1, GQ1
GQ1-C15	506543	1,270 ± 30	1,220 ± 42	Organic sediment	U5-2, GQ1
GQ1-C16	506544	12,440 ± 40	14,601 ± 173	Organic sediment	U4-1, GQ1
GQ1-C17	506545	8,340 ± 30	9,361 ± 57	Organic sediment	U4-1, GQ1
GQ2-C6	506548	3,100 ± 30	3,307 ± 45	Organic sediment	U4-2, GQ2
GQ2-C7	506549	2,030 ± 30	1,969 ± 44	Organic sediment	U4-2, GQ2
GQ2-C8	506550	920 ± 30	831 ± 49	Organic sediment	U5, GQ2
GQ2-C9	506551	9,120 ± 40	10,286 ± 57	Organic sediment	U2-2, GQ2
BQ-C1	532867	7,310 ± 30	8,104 ± 45	Organic sediment	U3, BQ
BQ-C2	532868	6,430 ± 30	7,359 ± 42	Organic sediment	U3, BQ
BQ-C3	532869	2,090 ± 30	2,054 ± 50	Organic sediment	U4, BQ
LCJ-C2	513060	1,470 ± 30	1,347 ± 25	Organic sediment	U3, XD

4.3.3.2 Event XE1

The youngest, most recent event occurred along faults f1 and f2 and faulted layers U1, U2 and U3. One colluvial wedge deposit W2 was rapidly formed along the f2 main fault plane and capped by layer U4. These characteristics suggest that the younger event occurred between the deposition of layers U3 and U4. To constrain the timing of this event, one soil sample (LCJ-C2) containing organic material was collected from the central sector of layer U3 for ^{14}C dating (Figure 4B). Based on the radiocarbon age, we suggest that the most recent event occurred after 1,347 ± 25 yr BP.

4.4 Radiocarbon dating of events

Numerous organic mud samples were collected in the above three trenches (Figures 7, 9, 12B) and one outcrop section (Figure 4B). Nineteen samples were sent to Beta Analytic Inc. for radiocarbon dating *via* the AMS method. Radiocarbon dates are summarized in Table 5. Most radiocarbon dates of the trench samples generally occurred in correct stratigraphic order, such that younger samples overlaid older samples. The ages of three samples were questionable (Figure 7): the age of sample GQ1-C7 (14,878 ± 152 yr BP) in U3-2 was older than that of GQ1-C4 (14,651 ± 166 yr BP) in underlying layer U2-1. Similarly, the age of GQ1-C16 (14,601 ± 173 yr BP) in U4-1 was older than that of GQ1-C6 (12,729 ± 16 yr BP), GQ1-C10 (12,745 ± 13 yr BP) and GQ1-C8 (14,143 ± 96 yr BP) in underlying layer U3-2, revealing obvious stratigraphic inversion. The age of sample GQ1-C8 (14,143 ± 96 yr BP) in layer U3-2 was much older than those of GQ1-C6 (12,729 ± 16 yr BP) and GQ1-C10 (12,745 ± 13 yr BP) in the same layer.

Inaddition, we observed that the ages of the above three samples, which were regarded as outliers, were all close to the age of sample collected from older strata. Specifically, the ages of samples GQ1-C7 (14,878 ± 152 yr BP), GQ1-C8 (14,143 ± 96 yr BP) and GQ1-C16 (14,601 ± 173 yr BP) were similar to that of GQ1-C4 (14,651 ± 165 yr BP). Therefore, we interpreted them as

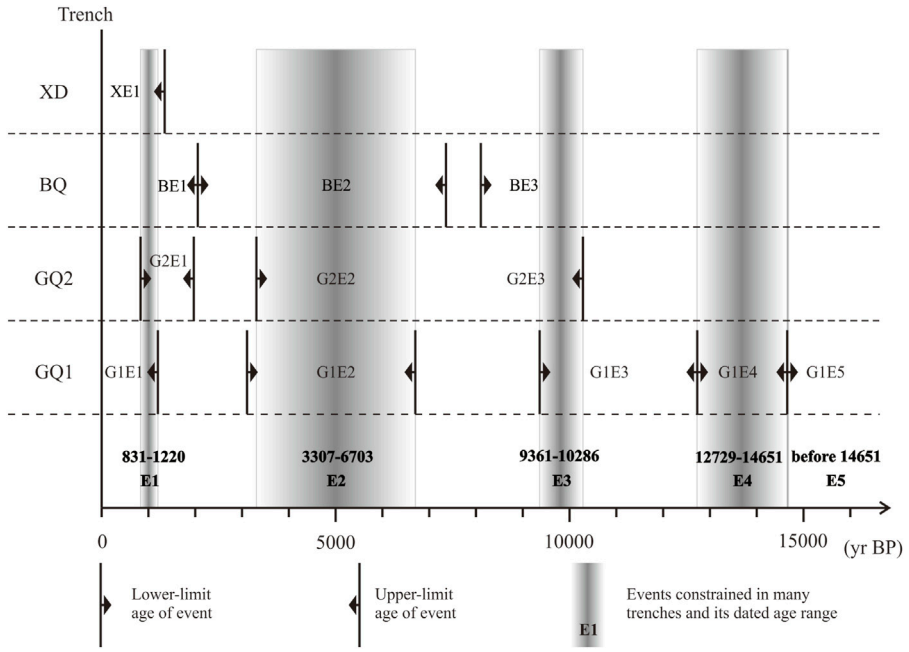

FIGURE 15
Constraints of the paleoseismic events and ages from the three trenches (GQ1, GQ2, and BQ) and one exposure (XD).

redeposited materials, and their ages represented early stratigraphic ages. The ages of these three samples were not used when constraining the ages of paleoearthquakes. Based on the ages of the other sixteen samples, we used the progressive confining method to constrain the timings of paleoseismic events recorded in the three trenches and one exposure. The constraint results are shown in Figure 15.

5 Discussion

5.1 Paleoseismic sequence and seismic recurrence behavior of the Yangda-Yaxu fault

Through trench excavations at the Guoqing and Bengqing sites, combined with one fault exposure at the Xudui site, five faulting events, named E5 through E1 from oldest to youngest, were identified at before 14,651, 12,729–14,651, 9,361–10,286, 3,307–6,703, and 831–1,220 yr BP, respectively (Figure 15). Unfortunately, due to the lack of recorded historical data in this region, no surface-faulting event in the Historical Strong Earthquake Catalog of China could be associated with the latest event (Science and Technology Committee of the Tibetan Autonomous Region, 1982; Department of Earthquake Disaster Prevention and State Seismological Bureau., 1995).

Based on the abovementioned event-constrained ages, the intervals between events E5, E4, E3, E2, and E1 were approximately >961, 3,866, 4,819, and 3,979 yr. Trenches GQ1 and GQ2 were excavated across the local low-lying area of the fault scarps, and trench BQ was excavated across sag pond. The excavation locations of the three trenches were all in a relative depositional environment rather than a denudation environment. Combined with the stratigraphic depositional sequence revealed by these trenches and one fault outcrop, we propose that the sedimentary sequence in this paper is likely relatively continuous, and the paleoseismic sequence may be relatively complete. If the events are complete, the recurrence interval of surface-faulting earthquakes along the YYF follows a quasi-periodic pattern with an interval of ~4,000 yr.

Despite the lack of strong earthquake records, the trench work in this paper revealed that at least five surface-rupturing events have occurred since the late Pleistocene. According to the horizontal coseismic displacement (~2–3 m) and the recurrence interval of the latest two earthquake events (~3,979 yr) obtained in this paper, we obtain a horizontal slip rate of ~0.5–0.8 mm/yr since the late Holocene.

5.2 Tectonic implications and the regional seismic risk

As mentioned above, the YYF cuts through the NF and the LCJF, which are ancient regional deep faults with a long and complex history of development and evolution, and divides them into two sections with significantly different activity levels.

Specifically, on the south side of YYF, both the NF and the LCJF are Holocene active faults. On the north side of YYF, the NF is active in the late Pleistocene, and the LCJF is active in the early and middle Pleistocene (Han, 2022a). Therefore, the YYF is an important fault structure in the region, which has a significant control effect on the late Quaternary evolution of the NF and the LCJF. Combining the clear linear geomorphic features along the fault and the paleoearthquake results in this paper, we believe that YYF is a newly-generated active fault with a relatively high maturity.

In recent years, the increasingly abundant observation data also shows that the interior of the QTB and CDB are not rigid and fixed, and many internal faults or local segments, for example, LTF, BTF, and BLF, also exhibit obvious Holocene activity characteristics and relatively strong seismogenic capacity, as evidenced from geological, paleoseismic, seismic data investigations (Gao, 2021; Wang et al., 2021; Han, 2022a; Han et al., 2022b; Ren et al., 2022b). For example, the BTF undergoes a dextral rate of ~1.3–2.7 mm/yr during late Quaternary (Zhou et al., 2005), and the LTF is a predominantly left-lateral strike-slip fault with a late Quaternary strike-slip rate ranging from ~2–4 mm/yr (Xu et al., 2005b; Zhou et al., 2005; Zhou et al., 2007). Our results reflect that the YYF is mainly a left-lateral strike-slip fault with a horizontal rate of ~0.5–0.8 mm/yr during the late Holocene, comparable to the BTF, LTF and other major faults within the QTB and CDB. Studies have shown that these faults have occurred multiple large earthquakes since the late Quaternary (Department of Earthquake Disaster Prevention and State Seismological Bureau., 1995; Zhou et al., 2005; Gao, 2021). The occurrence of strong earthquakes helped to release the accumulated strain energy attributed to Indian-Eurasian plate collision and accommodate the tectonic deformation associated with eastward extrusion of the upper crust of the Tibetan Plateau. Therefore, the active faults within the QTB and CDB, including YYF, play important role in accommodating crustal deformation, and should be given more attention when assessing the regional seismic risk and examining regional deformation in the future.

6 Conclusion

1) Our geomorphic observations and paleoseismic trenches demonstrated that the YYF is an active fault with a left-lateral strike-slip rate ranging from ~0.5–0.8 mm/yr since the late Holocene. At least five surface-faulting events with constrained ages ranging from before 14,651, 12,729–14,651, 9,361–10,286, 3,307–6,703, and 831–1,220 yr BP have occurred since the late Pleistocene. The recurrence interval of major earthquakes along the YYF follows a quasi-periodic pattern with an interval of ~4,000 yr.

2) The YYF is a newly-generated active fault. The fault has a significant control effect on the late Quaternary evolution of the NF and the LCJF, and also plays an important role in accommodating crustal deformation.

Data availability statement

The original contributions presented in the study are included in the article/supplementary material, further inquiries can be directed to the corresponding author.

Author contributions

The study was designed by LC, the field work was done by MH, YL, SG, JF, and LC, the writing and preparation of the original draft were conducted by MH, the review and editing of the finial manuscript were performed by LC and YL. All authors contributed to the article and approved the submitted version.

Funding

This research was supported financially by the Second Tibetan Plateau Scientific Expedition and Research Program (STEP) (2019QZKK0901); National Natural Science Foundation of China (41872228); and Basic Scientific Work of the Institute of Geology, China Earthquake Administration (IGCEA1418).

Acknowledgments

The authors greatly thank Associate Professor Hu Wang at the Faculty of Geosciences and Environmental Engineering, Southwest Jiaotong University, for his constructive and detailed comments to improve the manuscript. The authors also thank Peng Guo and Guodong Bao for their advice on our preliminary results.

Conflict of interest

The authors declare that the research was conducted in the absence of any commercial or financial relationships that could be construed as a potential conflict of interest.

The reviewer JR declared a shared affiliation with the authors MH, YL, SG, and JF to the handling editor at the time of review.

Publisher's note

References

Allen, C. R., Luo, Z. L., Qian, H., Wen, X. Z., Zhou, H. W., and Huang, W. S. (1991). Field study of a highly active fault zone: The Xianshuihe fault of southwestern China. *Geol. Soc. Am. Bull.* 103, 1178–1199. doi:10.1130/0016-7606(1991)103<1178:fsoaha>2.3.co;2

Bemis, S. P., Micklethwaite, S., Turner, D., James, M. R., Akciz, S., Thiele, S. T., et al. (2014). Ground-based and UAV-based photogrammetry: A multi-scale, high-resolution mapping tool for structural geology and paleoseismology. *J. Struct. Geol.* 69, 163–178. doi:10.1016/j.jsg.2014.10.007

Chang, Z. F., Zhang, Y. F., Li, J. L., and Zang, Y. (2014). The geological and geomorphic characteristic of late quaternary activity of the deqin-zhongdian-Daju fault (in Chinese with English abstract). *J. Seismol. Res.* 37 (1), 46–52. doi:10.3969/j.issn.1000-0666.2014.01.007

Chevalier, M. L., Leloup, P. H., Replumaz, A., Pan, J. W., Liu, D. L., Li, H. B., et al. (2016). Tectonic-geomorphology of the Litang fault system, SE Tibetan Plateau, and implication for regional seismic hazard. *Tectonophysics* 682, 278–292. doi:10.1016/j.tecto.2016.05.039

Deng, Q. D., Zhang, P. Z., Ran, Y. K., Yang, X. P., Min, W., and Chu, Q. Z. (2002). Basic characteristics of active tectonics of China (in Chinese). *Sci. China (Series D).* 32 (12), 1020–1030. doi:10.3321/j.issn:1006-9267.2002.12.007

Department of Earthquake Disaster PreventionState Seismological Bureau (1995). *Historical strong earthquake catalog of China (2300 BC-1911 AD.* Beijing: Seismological Publishing Press, 1–514. (in Chinese with English Abstract).

Gan, W. J., Zhang, P. Z., Shen, Z. K., Niu, Z. J., Wang, M., Wan, Y. G., et al. (2007). Present-day crustal motion within the Tibetan Plateau inferred from GPS measurements. *J. Geophys. Res.* 112 (B8), B08416. doi:10.1029/2005JB004120

Gao, M. X., Xu, X. W., Klinger, Y., Van der Woerd, J., and Tapponnier, P. (2017). High-resolution mapping based on an Unmanned Aerial Vehicle (UAV) to capture paleoseismic offsets along the Altyn-Tagh fault, China. *Sci. Rep.* 7 (1), 8281. doi:10.1038/s41598-017-081192

Gao, S. P. (2021). "Late Quaternary paleoseismology and faulting behavior of the internal and western boundary faults of Northwest Sichuan Subblock (in Chinese with English Abstract),". Ph.D. Thesis (Pakistan: Institute of Geology). China Earthquake Administration.

Guo, P., Han, Z. J., Dong, S. P., Mao, Z. B., Hu, N., Gao, F., et al. (2021). Latest quaternary active faulting and paleoearthquakes on the southern segment of the Xiaojiang fault zone, SE Tibetan plateau. *Lithosphere* 2021 (1). doi:10.2113/2021/7866379

Han, M. M., Chen, L. C., Li, Y, B., Gao, S. P., and Feng, J. H. (2022b). Geological and geomorphic evidence for late quaternary activity of the Bianba-Luolong fault on the western boundary of the Bangong-Nujiang suture (in Chinese with English abstract). *Eart. Scie.* 47 (3), 757–765. doi:10.3799/dqkx.2022.042

Han, M. M. (2022a). "Late quaternary activity of the bangda segment along the Nujiang fault zone (in Chinese with English abstract),". Ph.D. Thesis (Pakistan: Institute of Geology). China Earthquake Administration.

Li, D. Y., Chen, L. C., Liang, M. J., Gao, S. P., Zeng, D., Wang, H., et al. (2017). Holocene paleoseismologic record and rupture behavior of large earthquake on the Xianshuihe fault (in Chinese with English Abstract). *Seismol. Geol.* 39 (4), 623–643. doi:10.3969/j.issn.0253-4967.2017.04.001

Li, Y. J., Liu, M., Li, Y. H., and Chen, L. W. (2019). Active crustal deformation in southeastern Tibetan Plateau: The kinematics and dynamics. *Earth Planet. Sci. Lett.* 523, 115708. doi:10.1016/j.epsl.2019.07.010

Liang, M. J. (2019). "Characteristics of the late Quaternary fault activity of the Xianshuihe fault (in Chinese with English abstract),". Ph.D. Thesis (Pakistan: Institute of Geology). China Earthquake Administration.

Liang, M. J., Chen, L. C., Ran, Y. K., Li, Y. B., Gao, S. P., Han, M. M., et al. (2020b). Abnormal accelerating stress release behavior on the Luhuo segment of the Xianshuihe fault, southeastern margin of the Tibetan plateau, during the past 3000 years. *Front. Earth Sci. (Lausanne).* 8, 274. doi:10.3389/feart.2020.00274

Liang, M. J., Yang, Y., Du, F., Gong, Y., Sun, W., Zhao, M., et al. (2020a). Late Quaternary activity of the central segment of the Dari fault and restudy of the surface rupture zone of the 1947 *M* 7¾ Dari earthquake, Qinghai Province. *Seismol. Geol.* 42, 703–714. doi:10.3969/j.issn.0253-4967.2020.03.011

Liu-Zeng, J., Klinger, Y., Xu, X. W., Lasserre, C., Chen, G. H., Chen, W. B., et al. (2007). Millennial recurrence of large earthquakes on the Haiyuan fault near Songshan, Gansu province, China. *Bull. Seismol. Soc. Am.* 97 (1B), 14–34. doi:10.1785/0120050118

McCalpin, J. P. (2009). *Paleoseismology*. San Diego, California: Academic Press.

Ramsey, C. B. (2009). Bayesian analysis of radiocarbon dates. *Radiocarbon* 51 (1), 337–360. doi:10.1017/s0033822200033865

Ran, Y. K., Wang, H., Li, Y. B., and Chen, L. C. (2012). Key techniques and several cases analyses in paleoseismic studies in mainland China (1): Trenching sites, layouts, and paleoseismic indicators on active strike-slip faults (in Chinese with English abstract). *Seismol. Geol.* 34 (2), 197–210. doi:10.3969/j.issn.0253-4967.2012.02.001

Reimer, P. J., Bard, E., Bayliss, A., Beck, J. W., Blackwell, P. G., Ramsey, C. B., et al. (2013). IntCal13 and Marine13 radiocarbon age calibration curves 0-50, 000 years cal BP. *Radiocarbon* 55 (4), 1869–1887. doi:10.2458/azu_js_rc.55.16947

Ren, J. J., Xu, X., Lv, Y., Wang, Q., Li, A., Li, K., et al. (2022b). Late Quaternary slip rate of the northern Lancangjiang fault zone in eastern Tibet: Seismic hazards for the Sichuan-Tibet Railway and regional tectonic implications. *Eng. Geol.* 306, 106748. doi:10.1016/j.enggeo.2022.106748

Ren, J. J., Xu, X. W., Yeats, R. S., Zhang, S. M., Ding, R., and Gong, Z. (2013). Holocene paleoearthquakes of the Maoergai fault, eastern Tibet. *Tectonophysics* 590, 121–135. doi:10.1016/j.tecto.2013.01.017

Ren, J. J., Xu, X. W., Zhang, G. W., Wang, Q. X., Zhang, Z. W., Gai, H. L., et al. (2022a). Coseismic surface ruptures, slip distribution, and 3D seismogenic fault for the 2021 Mw 7.3 Maduo earthquake, central Tibetan Plateau, and its tectonic implications. *Tectonophysics* 827 (229275). doi:10.1016/j.tecto.2022.229275

Ren, J. J., Xu, X. W., Zhang, S. M., Yeats, R. S., Chen, J. W., Zhu, A. L., et al. (2018). Surface rupture of the 1933 M 7.5 Diexi earthquake in eastern Tibet: Implications for seismogenic tectonics. *Geophys. J. Int.* 212, 1627–1644. doi:10.1093/gji/ggx498

Science and Technology Committee of the Tibetan Autonomous Region (in Chinese) (1982). *Records of historical earthquakes of Tibet*. Lhasa: People's Press of the Tibet.

Sun, H. Y., He, H. L., Ikeda, Y., Kano, K., Shi, F., Gao, W., et al. (2015). Holocene paleoearthquake history on the Qingchuan fault in the northeastern segment of the Longmenshan Thrust Zone and its implications. *Tectonophysics* 660, 92–106. doi:10.1016/j.tecto.2015.08.022

Sun, H. Y., He, H. L., Wei, Z. Y., Shi, F., and Gao, W. (2017). Late Quaternary paleoearthquakes along the northern segment of the Nantinghe fault on the southeastern margin of the Tibetan Plateau. *J. Asian Earth Sci.* 138 (MAY1), 258–271. doi:10.1016/j.jseaes.2017.02.023

Tapponnier, P., Xu, Z. Q., Roger, F., Meyer, B., Arnaud, N., Wittlinger, G., et al. (2001). Oblique stepwise rise and growth of the Tibet Plateau. *Science* 294 (5547), 1671–1677. doi:10.1126/science.105978

Taylor, M., and Yin, A. (2009). Active structures of the Himalayan-Tibetan orogen and their relationships to earthquake distribution, contemporary strain field, and Cenozoic volcanism. *Geosph. (Boulder).* 5 (3), 199–214. doi:10.1130/GES00217.1

Wang, H., Li, K. J., Chen, L. C., and Li, A. (2020). Evidence for Holocene activity on the Jiali fault, an active block boundary in the southeastern Tibetan Plateau. *Seismol. Res. Lett.* 91 (3), 1776–1780. doi:10.1785/0220190371

Wang, H., Ran, Y. K., Li, Y. B., Gomez, F., and Chen, L. C. (2013). Holocene palaeoseismologic record of earthquakes on the Zemuhe fault on the southeastern margin of the Tibetan Plateau. *Geophys. J. Int.* 193, 11–28. doi:10.1093/gji/ggs095

Wang, M., and Shen, Z. K. (2020). Present-Day crustal deformation of continental China derived from GPS and its tectonic implications. *J. Geophys. Res. Solid Earth* 125. doi:10.1029/2019JB018774

Wang, S. Y., Zhou, R. J., Liang, M. J., Liu, S., Liu, N. N., and Long, J. Y. (2021). Co-seismic surface rupture and recurrence interval of large earthquakes along damaoyaba-litang segment of the Litang fault on the eastern margin of the Tibetan plateau in China. *J. Earth Sci.* 32, 1139–1151. doi:10.1007/s12583-021-1425-z

Wen, X. Z., Ma, S. L., Xu, X. W., and He, Y. N. (2008). Historical pattern and behavior of earthquake ruptures along the eastern boundary of the Sichuan-Yunnan faulted-block, southwestern China. *Phys. Earth Planet. Interiors* 168 (1-2), 16–36. doi:10.1016/j.pepi.2008.04.013

Xu, X. W., Wen, X. Z., Yu, G. H., Zheng, R. Z., Luo, H. Y., and Zheng, B. (2005a). Average slip rate, earthquake rupturing segmentation and recurrence behavior on the Litang fault zone, western sichuan ?rovince, China (in Chinese with English abstract). *Sci. China Ser. D Earth Sci.* 48 (8), 540–551.

Xu, X. W., Wen, X. Z., Zheng, R. Z., Ma, W. T., Song, F. M., and Yu, G. H. (2003). Pattern of latest tectonic motion and its dynamics for active blocks in Sichuan-Yunnan region, China (in Chinese with English Abstract). *Sci. China (Series D)* 33, 151–162.

Xu, X. W., Zhang, P. Z., Wen, X. Z., Qin, Z. L., Chen, G. H., and Zhu, A. L. (2005b). Features of active tectonics and recurrence behaviors of strong earthquakes in the western Sichuan Province and its adjacent regions (in Chinese with English Abstract). *Seismol. Geol.* 27 (3), 446–461.

Yin, A., and Harrison, T. M. (2000). Geologic evolution of the Himalayan-Tibetan orogen. *Annu. Rev. Earth Planet. Sci.* 28, 211–280. doi:10.1146/annurev.earth.28.1.211

Yuan, Z. D., Li, T., Su, P., Sun, H. Y., Ha, G. H., Guo, P., et al. (2022). Large surface-rupture gaps and low surface fault slip of the 2021 M_w 7.4 Maduo earthquake along a low-activity strike-slip fault, Tibetan Plateau. *Geophys. Res. Lett.* 49, e2021GL096874. doi:10.1029/2021GL096874

Zhan, Y., Liang, M. J., Sun, X. Y., Huang, F. P., Zhao, L. Q., Gong, Y., et al. (2021). Deep structure and seismogenic pattern of the 2021. 5. 22 madoi (qinghai) ms 7.4 earthquake (in Chinese with English abstract). *Chin. J. Geophys.* 64 (7), 2232–2252. doi:10.6038/cjg2021O0521

Zhang, L., Liang, S. M., Yang, X. P., Gan, W., and Dai, C. (2021). Geometric and kinematic evolution of the Jiali fault, eastern Himalayan Syntaxis. *J. Asian Earth Sci.* 212, 104722. doi:10.1016/j.jseaes.2021.104722

Zhang, P. Z., Deng, Q. D., Zhang, G. M., Ma, J., Gan, W. J., Min, W., et al. (2003). China continental strong earthquake activities and active blocks (in Chinese). *Sci. China Ser. D Earth Sci.* 33, 12–20.

Zhang, P. Z., Shen, Z. K., Wang, M., Gan, W. J., Bürgmann, R., Molnar, P., et al. (2004). Continuous deformation of the Tibetan Plateau from global positioning system data. *Geol.* 32 (9), 809–812. doi:10.1130/G20554.1

Zhou, C. J., Wu, Z. H., Zhang, K. Q., Li, J., Jiang, Y., Tian, T., et al. (2015). New chronological constraint on the co-seismic surface rupture segments associated with the Litang fault (in Chinese with English Abstract). *Seismol. Geol.* 37 (2), 455–467. doi:10.3969/j.issn.0253-4967.2015.02.009

Zhou, R. J., Chen, G. X., Li, Y., Zhou, C. H., Gong, Y., He, Y. L., et al. (2005). Research on active faults in litang-batang region, western sichuan ?rovince, and the seismogenic structures of the 1989 Batang M 6.7 earthquake swarm (in Chinese with English abstract). *Seismol. Geol.* 27 (1), 31–43. doi:10.3969/j.issn.0253-4967.2005.01.004

Zhou, R. J., Ye, Y. Q., Li, Y., Li, X. G., He, Y. L., and Ge, T. Y. (2007). Late-quaternary activity of the shawan segment of the Litang faults (in Chinese with English abstract). *Quat. Sci.* 27 (1), 45–53. doi:10.3321/j.issn:1001-7410.2007.01.006